RSC Advances

PAPER

View Article Online
View Journal | View Issue

Cite this: *RSC Adv.*, 2021, **11**, 39045

Realizing high performance flexible supercapacitors by electrode modification†

Tong Xia,[a] Depeng Zhao,[a] Qing Xia,[a] Ahmad Umar[c] and Xiang Wu *[ab]

Received 26th October 2021
Accepted 2nd December 2021

DOI: 10.1039/d1ra07880a

rsc.li/rsc-advances

It is well known that the structure of an electrode material seriously affects its electrochemical performance. In this study, we prepare hybrid structured $NiCo_2S_4$@PPy nanoarchitectures by a hydrothermal method and subsequent electrodeposition process. The specific capacitance of the obtained sample is 1733.23 C g^{-1} at 1 A g^{-1}. The assembled asymmetric device presents an energy density of 59.59 W h kg^{-1} at 1404.04 W kg^{-1}. The excellent electrochemical performance can be attributed to the synergistic effect between the high theoretical specific capacitance of the $NiCo_2S_4$ sheets and the superior cycling stability of the PPy film. The device also shows an outstanding mechanical flexibility at different bending angles.

Introduction

Among various emerging energy storage devices, supercapacitors have been the focus of research due to their fast charge transfer capability, excellent cycle life and outstanding power density.[1–3] However, low energy density limits their further applications.[4–6] In general, the inherent characteristics of electrode materials are key factors, such as microstructure, specific surface area and electrical conductivity. These determine their total electrochemical performance.[7,8] Therefore, designing electrode materials with unique structures is an effective strategy to increase the energy density.[9–12]

Transition metal sulfides are receiving increasing attention due to their high electrical conductivity and superior structural stability.[13–15] Compared with single metal sulfides, mixed metal sulfides show rich redox reactions, which significantly improve the electrochemical performance of the device.[16–18] However, the brittle feature of transition metal sulfides means they tend to collapse during long-term cycling, which further hinders their practical application.[19–21]

Hybrid electrode structures formed by combining sulfides and other electrode materials are considered as a feasible way to improve the electrochemical performance.[22] PPy is widely used as a capacitor material due to its superior electrical conductivity and cycling performance.[23] Zheng's group prepared PPy@$NiCo_2S_4$ core–shell heterostructures with PPy nanotubes as the backbone and $NiCo_2S_4$ sheets as the shell. It delivers a specific capacitance of 908.1 F g^{-1} at 1 A g^{-1}.[24] Zhu and coworkers used metal organic frameworks (MOFs) to synthesize $ZnCo_2O_4$@$NiCo_2S_4$@PPy core–shell nanosheets on nickel foam. The samples present a specific capacitance of 2507.0 F g^{-1} at 0.5 A g^{-1}.[25] Yi *et al.* prepared $NiCo_2S_4$@PPy stacked structures by a facile synthesized process, which shows a capacitance of 1606.6 F g^{-1} at 1 A g^{-1} and a cycle stability after 20 000 cycles.[26]

Herein, we synthesize $NiCo_2S_4$ nanosheets on nickel foam substrate by a two-step hydrothermal method. Then a layer of PPy film is covered on the surface of $NiCo_2S_4$ sample by an electrodeposition process. Due to the unique structural feature, the obtained product shows a specific capacitance of 1733.23 C g^{-1} at 1 A g^{-1}. After 10 000 cycles at 20 A g^{-1}, there is still 78% capacitance retention. An asymmetric supercapacitor is assembled with $NiCo_2S_4$@PPy sample as positive electrode and active carbon as negative one. It presents an energy density of 59.59 W h kg^{-1} at 1404.04 W kg^{-1}. Furthermore, the asymmetric devices possess superior mechanical flexibility at different bending angles.

Results and discussion

Fig. 1 shows the synthesis process of $NiCo_2S_4$@PPy nanosheets on nickel foam. $NiCo_2S_4$ electrode material is prepared by a two-step hydrothermal method. Firstly, in aqueous solution, Ni^{2+} and Co^{2+} are deposited on the surface of nickel foam by electrostatic force to form Ni–Co precursors. Secondly, Na_2S as a sulfur source is hydrolyzed to form HS^- and H_2S, which react with the precursor to obtain $NiCo_2S_4$ nanosheets. Afterwards, a layer of PPy film is deposited on the surface of $NiCo_2S_4$ product by an electrodeposition process at different time. The chemical reactions involved in the synthesis process are expressed as follows:

[a]School of Materials Science and Engineering, Shenyang University of Technology, Shenyang 110870, P. R. China. E-mail: wuxiang05@163.com; wuxiang05@sut.edu.cn
[b]Key Laboratory of Advanced Energy Materials Chemistry (Ministry of Education), College of Chemistry, Nankai University, Tianjin 300071, P. R. China
[c]Department of Chemistry, College of Science and Arts, Promising Centre for Sensors and Electronic Devices (PCSED), Najran University, Najran 11001, Saudi Arabia

† Electronic supplementary information (ESI) available. See DOI: 10.1039/d1ra07880a

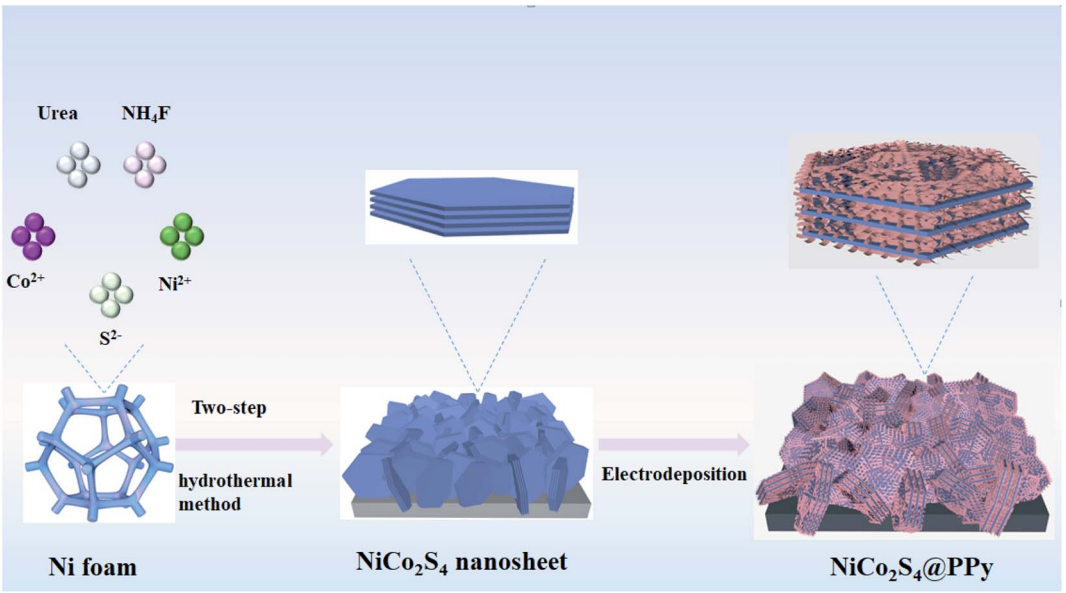

Fig. 1 Synthetic schematic of $NiCo_2S_4$@PPy nanosheet composite.

$$Ni^{2+} + 2Co^{2+} + 4S^{2-} + 1/2O_2 + H_2O = NiCo_2S_4 + 2OH^- \quad (1)$$

XRD patterns of the synthesized samples are shown in Fig. 2a. Clearly, three strong peaks are assigned to nickel substrate. The diffraction peaks at 2θ values of 31.59°, 38.32°, 50.46°, 69.29° and 78.15° correspond to the (311), (400), (511), (440) and (731) crystal planes of the cubic spinel $NiCo_2S_4$ phase (JCPDS no. 20-0782). Besides, several diffraction peaks of Ni_3S_2 and Ni_9S_8 are also detected, indicating that the samples are partly vulcanized. For $NiCo_2S_4$@PPy composite, no excess peaks are observed due to the amorphous nature of PPy and its low content.

The surface structural information of $NiCo_2S_4$@PPy samples is further analyzed by XPS. Ni 2p spectra (Fig. 2b) show two spin orbitals Ni $2p_{1/2}$ and Ni $2p_{3/2}$, accompanied by a distinct shaking satellite peak (labeled "Sat."). The two peaks with binding energies of 857.3 and 875.2 eV correspond to Ni^{3+}, while another two peaks with binding energies of 855.8 and 873.5 eV can be assigned to Ni^{2+}. It proves the presence of Ni^{2+} and

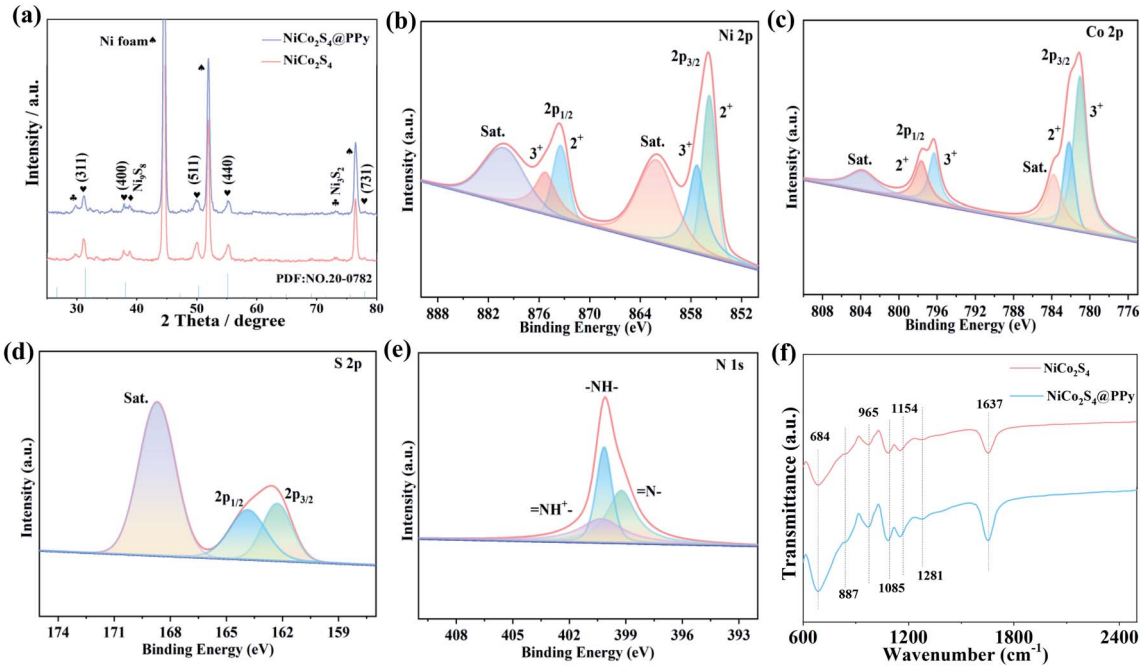

Fig. 2 Structural characterization (a) XRD patterns (b) Ni 2p (c) Co 2p (d) S 2p and (e) N 1s XPS spectra (f) FTIR spectra.

Ni^{3+}.[27,28] For the Co 2p spectra (Fig. 2c), the peaks at 780.9 eV and 796.3 eV are Co^{3+}, while 782.2 eV and 797.7 eV are attributed to Co^{2+}. It shows that Co^{2+} and Co^{3+} participate in redox reactions together.[29] As shown in Fig. 2d, the diffraction peaks at 162.3 eV and 163.9 eV are relative with S $2p_{3/2}$ and S $2p_{1/2}$.[30] From Fig. 2e, the peaks of N 1s are located at binding energies of 399.2, 400.1 and 400.5 eV, which belong to imine nitrogen (=N–), pyrrole nitrogen (–NH–) and positively charged nitrogen ($–NH^+–$), respectively.[31]

FTIR tests are also performed to verify the presence of PPy in $NiCo_2S_4$@PPy sample. The characteristic peaks consist of 684, 887, 965, 1085, 1154, 1281 and 1637 cm^{-1}, as shown in Fig. 2f. Among them, the bond at 684 cm^{-1} is related to the deformation of the outer ring of the C–C plane.[26] The peaks at 887, 1085, 1154, and 1281 cm^{-1} are thought to be deformation vibrations in the C–H or C–N plane.[32,33] The C=C and C=O bending vibrations correspond to the peaks at 965 and 1637 cm^{-1}, respectively.[34,35] These results indicate successfully wrapping of PPy film on $NiCo_2S_4$ samples.

The morphology of the samples can be obtained by SEM. Fig. 3a shows that many nanosheets are uniformly distributed on nickel foam. The thickness of each nanosheets is 100 nm (Fig. 3b). SEM images of $NiCo_2S_4$@PPy-50 sample are shown in Fig. 3c and d. It is found that the structure of nanosheet remains unchanged, indicating that PPy film does not affect the structure of the sample (Fig. 3c). From SEM images (Fig. 3d), PPy film is successfully deposited onto $NiCo_2S_4$ nanosheets. SEM images of $NiCo_2S_4$@PPy-30 and $NiCo_2S_4$@PPy-70 samples are shown in Fig. S1.† One finds that the thickness of PPy film varies with difference of electrodeposition time.

Further structural information of the $NiCo_2S_4$@PPy-50 product is studied by TEM characterization. In Fig. 3e, the sample consists of some nanosheets stacked up. Moreover, a layer of PPy film can be seen, which is covered on the surface of nanosheet. The average thickness of PPy film is 9 nm. In HRTEM image (Fig. 3f), the measured 0.28 nm lattice distance belongs to the (311) crystal plane of $NiCo_2S_4$. SAED pattern in inset shows continuous diffraction ring, revealing the polycrystalline nature. In addition, the elemental mapping images show that Ni, Co, S and N elements are uniformly distributed (Fig. 3g).

Then we investigate the electrochemical properties of the prepared samples. CV curves of the products are obtained in a potential window of 0–0.6 V at 10 mV s^{-1}, as shown in Fig. 4a. Compared with other electrode materials, the closed curve area of $NiCo_2S_4$@PPy-50 electrode is the biggest at the same scan rate, indicating its excellent charge storage capacity. Fig. 4b shows the GCD curves of several samples at 1 A g^{-1}. It is clearly observed that the discharge time of $NiCo_2S_4$@PPy-50 product is longer than those of several other products, demonstrating the

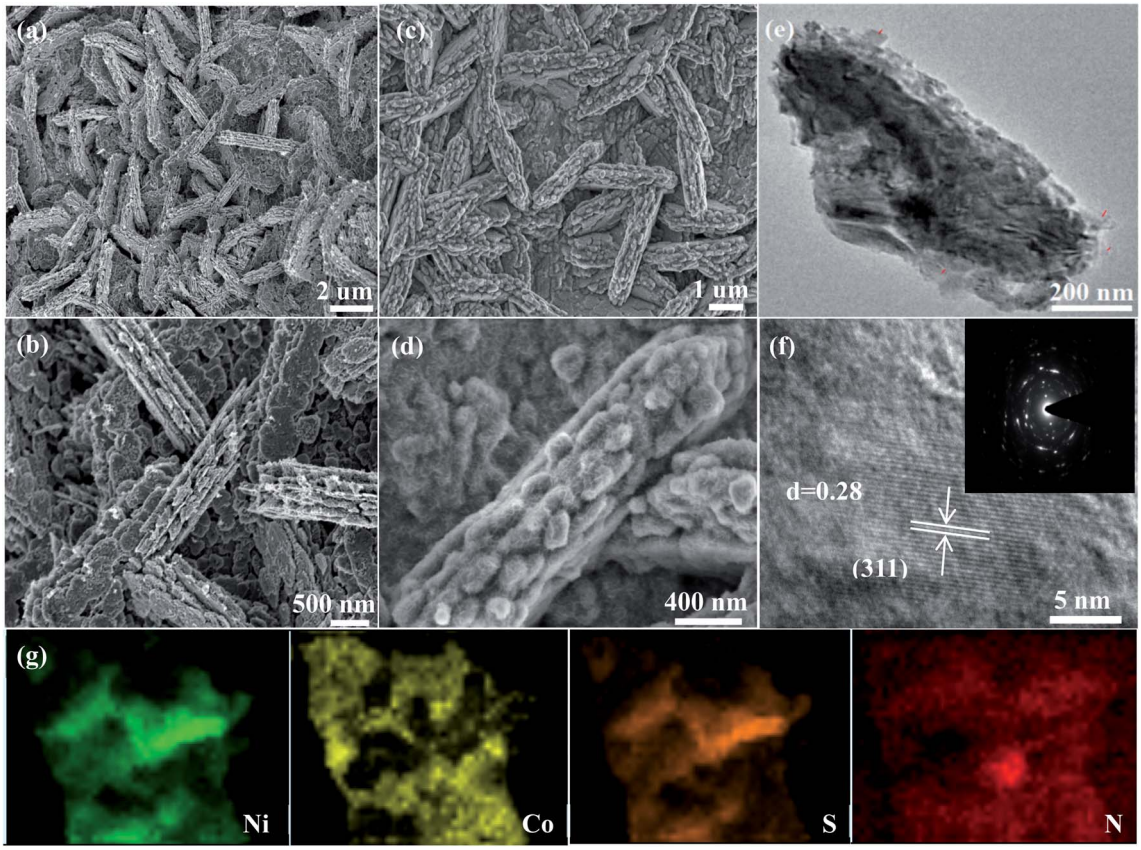

Fig. 3 Morphology characterization (a and b) SEM images of $NiCo_2S_4$ samples (c and d) SEM images of $NiCo_2S_4$@PPy-50 samples (e) TEM image (f) HRTEM image and SAED pattern (g) elemental mapping images.

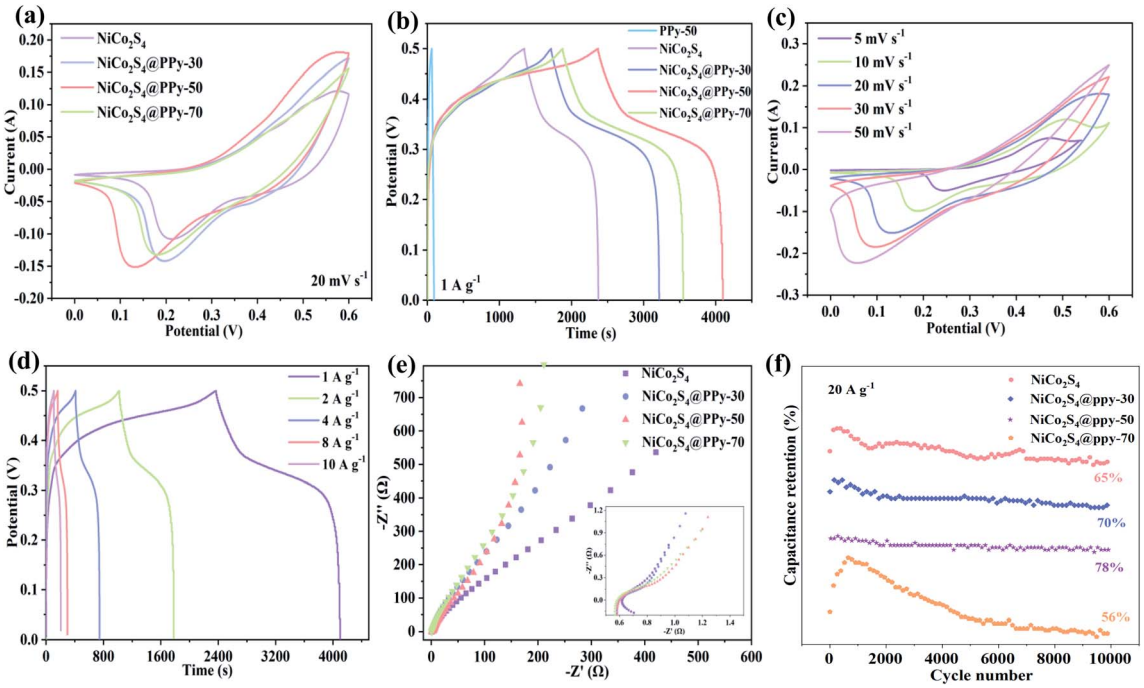

Fig. 4 Electrochemical performance (a) CV curves (b) GCD curves (c) CV curves of $NiCo_2S_4$@PPy-50 samples (d) GCD curves of $NiCo_2S_4$@PPy-50 samples (e) Nyquist plots (f) cycling performance.

high specific capacitance feature. We also obtain the specific capacitances of 31.85, 975.64 and 1733.23 C g^{-1} for PPy-50, $NiCo_2S_4$ and $NiCo_2S_4$@PPy-50 samples at a current density of 1 A g^{-1}, respectively. The results show that the specific capacitance of the $NiCo_2S_4$@PPy-50 electrode material is higher than the sum of the specific capacitance of $NiCo_2S_4$ and PPy samples, implying that the synergistic effect makes it possess excellent electrochemical performance.

CV curves of $NiCo_2S_4$@PPy-50 samples at 5 to 50 mV s^{-1} are shown in Fig. 4c. With the increase of sweep speed, the shapes of curves remain almost constant, revealing their superior reversibility. The redox process in alkaline electrolyte can be expressed by the following equation:

$$NiS + OH^- = NiSOH + e^- \quad (2)$$

$$CoS + OH^- = CoSOH + e^- \quad (3)$$

$$CoSOH + OH^- = CoSO + H_2O + 2e^- \quad (4)$$

Fig. 4d presents GCD curves of $NiCo_2S_4$@PPy-50 samples at different current densities. An obvious platform indicates their Faraday redox behavior. Specific capacitance of $NiCo_2S_4$@PPy-50 product at 1 to 10 A g^{-1} is 1733.23, 1512.22, 1320.40, 1015.68 and 949.90 C g^{-1}, respectively. CV and GCD curves of several other samples are also shown in Fig. S2.† High symmetric curves show the outstanding electrochemical reversibility.

Electrochemical impedances of the samples are then investigated in frequency range from 0.01 Hz to 100 kHz, as shown in Fig. 4e. Distinct semicircles (in high frequency region) and straight lines (low frequency region) can be observed, respectively. The radius of semicircle represents charge transfer resistance, and the slope of straight line refers diffusion resistance, that is the rate of electrolyte ion transfer.[36] Semicircle of $NiCo_2S_4$@PPy-50 product is significantly smaller than those of other three electrodes. Its slope is the largest, indicating that it possesses the smallest resistance. The capacitance retention of $NiCo_2S_4$@PPy-50 sample is 78% after 10 000 cycles at 20 A g^{-1}. We propose that the excellent cycle stability benefits to the unique stacking structures of nanosheets, which alleviate volume expansion of electrode during cycling. The capacitance retention of $NiCo_2S_4$, $NiCo_2S_4$@PPy-30 and $NiCo_2S_4$@PPy-70 samples are 65%, 70% and 56%, respectively (Fig. 4f). For the rapid increase in the first 1000 cycles, it may be due to the long deposition time and the increase in the thickness of PPy, which leads to an increase in the activation time.

To study practical applications of the synthesized product, we assemble an asymmetric supercapacitor using $NiCo_2S_4$@PPy-50 sample as positive electrode and activated carbon as negative one. CV curves of positive and negative electrode at 20 mV s^{-1} are shown in Fig. 5a. Their potential windows are 0–0.6 V, and −1–0 V, respectively. GCD curves at different voltage windows (Fig. 5b) show that the device can still operate stably at a voltage window of 1.56 V. CV curves (Fig. 5c) at different scanning speeds are quasi-rectangular shapes, demonstrating the co-existence of electric double layer and pseudo-capacitance characteristics.[37] The shapes does not change as sweep speed increases, indicating that the shapes of CV curve are not sensitive to the redox reaction process. The highly symmetrical charge and discharge curves in Fig. 5d indicate the electrode materials possess excellent electrochemical reversibility.

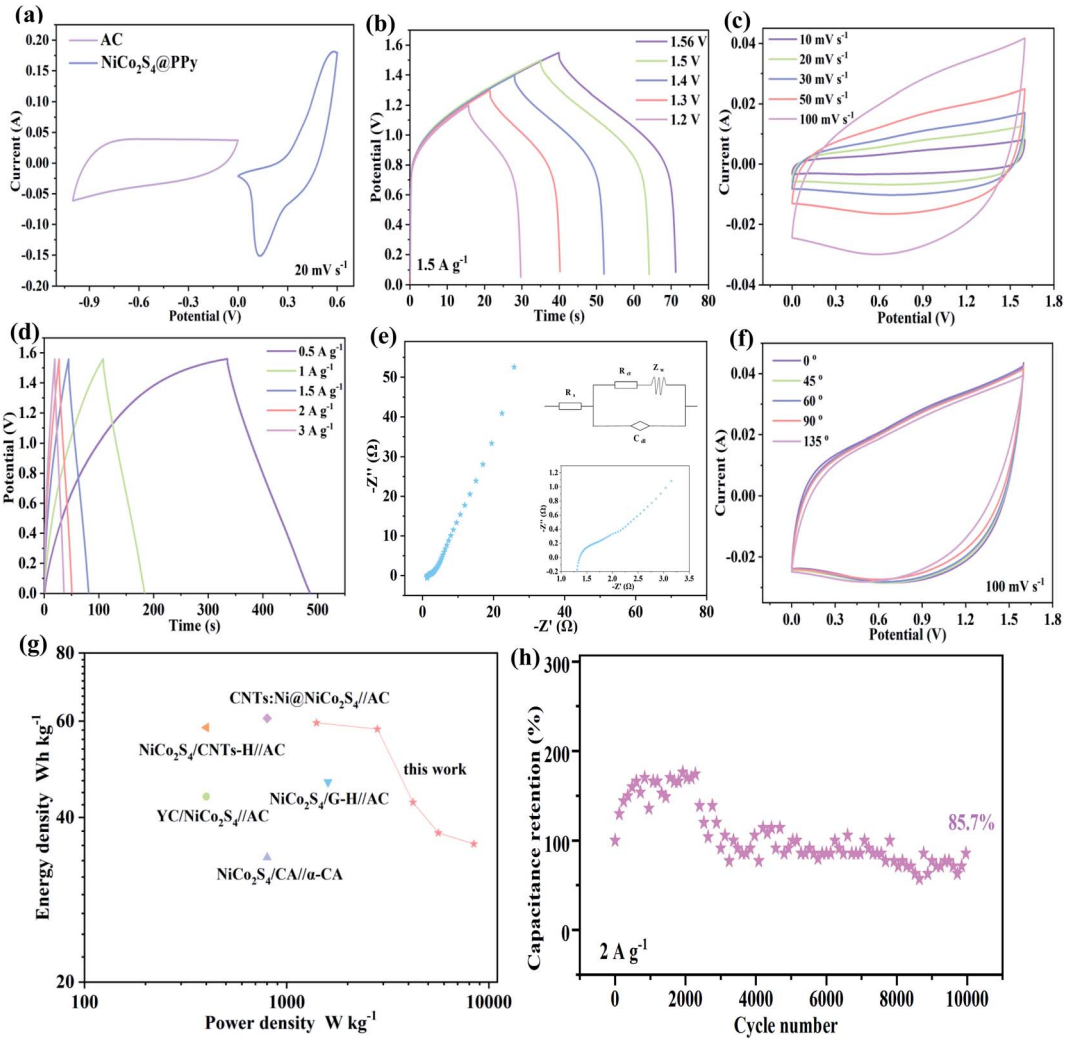

Fig. 5 Electrochemical properties of the asymmetric device (a) CV curves (b) GCD curves in different potential windows (c) CV curves at various scanning rates (d) GCD curves at various current density (e) Nyquist plot (f) CV curves at different bending angles (g) Ragone plot (h) cycling performance.

According to calculation, the specific capacitance of the device is 76.40, 74.38, 54.68, 48.06 and 45.87 C g^{-1} at 0.5 to 3 A g^{-1}, respectively. We performed OCPT measurements for the assembled devices to confirm self-discharge and leakage current. From Fig. S3(a),† it can be found that the voltage exhibits a relative long stability. However, in the initial stage at a range from 0.1736 to 0.1743 V, the voltage shows a clear increase, which leads to the asymmetric behavior. This phenomenon is consistent with the GCD curves of the device. The corresponding i_R value is calculated according to Fig. 5d, as shown in Fig. S3(b),† from which it can be seen that there is a nonlinear relationship between potential and voltage, indicating that the material is intrinsically less active and less conductive. Moreover, the equivalent resistance value after assembly is 1.3 Ω (Fig. 5e), and the small resistance value implies that asymmetric device shows excellent charge transfer kinetics. Equivalent circuit diagrams of several resistors are shown in the illustration.

In order to explore the flexibility of the device, we bend and fold it at different angles, and the digital photos are shown in Fig. S4.† CV curves of device at different bending angles (Fig. 5f) show that the enclosed area remains almost unchanged. It implies its outstanding mechanical stability.[38] The Ragone plot of the device is shown in Fig. 5g. The assembled $NiCo_2S_4$@PPy-50//AC device presents an energy density of 59.59 W h kg^{-1} at 1404.05 W kg^{-1}. It is better than some previous reports.[39–43] Furthermore, 85.7% capacitance retention is achieved after 10 000 cycles at 2 A g^{-1} (Fig. 5h).

Conclusions

In summary, we have prepared several $NiCo_2S_4$@PPy nanosheet composites by facile synthesis routes. The unique 2D structures of $NiCo_2S_4$ nanosheets provide abundant active sites, which is conducive to many redox reactions. The excellent conductivity of PPy film ensures the rapid transport of electrolyte ions and even then achieves outstanding charge transfer kinetics

behaviors. Moreover, due to the synergistic effect between multiple components, the specific capacitance is significantly increased. In addition, the assembled $NiCo_2S_4$@PPy-50//AC asymmetric device possesses high energy density and excellent mechanical stability. It demonstrates future applications in some flexible energy storage devices.

Conflicts of interest

There are no conflicts to declare.

References

1 B. Liu, S. Sun, R. Y. Jia, H. S. Zhang, X. H. Zhu, C. G. Zhang, J. Xu, T. Zhai and H. Xia, *Adv. Funct. Mater.*, 2020, **30**, 1909546.
2 Q. Y. Gui, L. X. Wu, Y. Y. Li and J. P. Liu, *Adv. Sci.*, 2019, **6**, 1802067.
3 Y. H. Wang, R. N. Liu, Y. D. Tian, Z. Sun, Z. H. Huang, X. L. Wu and B. Li, *Chem. Eng. J.*, 2020, **384**, 123263.
4 M. Z. Dai, D. P. Zhao and X. Wu, *Chin. Chem. Lett.*, 2020, **31**, 2177–2188.
5 L. Wan, Y. L. Yuan, J. X. Liu, J. Chen, Y. Zhang, C. Du and M. J. Xie, *Electrochim. Acta*, 2021, **368**, 137579.
6 H. Q. Liu, D. P. Zhao, Y. Liu, Y. L. Tong, X. Wu and G. Z. Shen, *Sci. China Mater.*, 2020, **64**, 581–591.
7 C. Liu, X. Wu and B. Wang, *Chem. Eng. J.*, 2020, **392**, 123651.
8 W. F. Liu, P. G. Liu, R. Hao, Y. P. Huang, X. X. Chen, R. Z. Cai, J. Yan and K. Y. Liu, *ChemElectroChem*, 2020, **7**, 1166–1171.
9 C. Long, L. Miao, D. Z. Zhu, H. Duan, Y. K. Lv, L. C. Li, M. X. Liu and L. H. Gan, *ACS Appl. Energy Mater.*, 2021, **4**, 5727–5737.
10 Y. Liu and X. Wu, *Nano Energy*, 2021, **86**, 106124.
11 Z. Y. Song, L. Miao, L. C. Li, D. Z. Zhu, L. H. Gan and M. X. Liu, *Carbon*, 2021, **180**, 135–145.
12 Y. Li, P. Kamdemb and X. J. Jin, *Dalton Trans.*, 2020, **49**, 7807–7819.
13 P. F. Hu, Y. Liu, H. Q. Liu, X. Wu and B. D. Liu, *ACS Appl. Nano Mater.*, 2021, **4**, 2183–2189.
14 D. Wang, L. Y. Tian, J. Y. Huang, D. W. Li, J. Y. Liu, Y. Xu, H. Z. Ke and Q. F. Wei, *Electrochim. Acta*, 2020, **334**, 135636.
15 D. P. Zhao, M. Z. Dai, Y. Zhao, H. Q. Liu, Y. Liu and X. Wu, *Nano Energy*, 2020, **72**, 104715.
16 K. Sekar, G. Raji, S. Y. Chen, S. H. Liu and R. M. Xing, *Appl. Surf. Sci.*, 2020, **527**, 146856.
17 T. Xia, Y. Liu, M. Z. Dai, Q. Xia and X. Wu, *Dalton Trans.*, 2021, **50**, 4045–4052.
18 Y. S. Gai, T. Xie, Y. Y. Shang, L. H. Su, J. Wang and L. Y. Gong, *Energy Fuels*, 2020, **34**, 10203–10210.
19 Y. Liu, D. P. Zhao, H. Q. Liu, A. Umar and X. Wu, *Chin. Chem. Lett.*, 2019, **30**, 1105–1110.
20 Y. K. Liu, G. H. Jiang, B. Yu, U. Evariste and P. P. Ma, *J. Alloys Compd.*, 2020, **832**, 154909.
21 X. Zhou, H. Dai, X. Huang, Y. Ren, Q. Wang, W. Wang, W. Huang and X. Dong, *Mater. Today Energy*, 2020, **17**, 100429.
22 M. Z. Dai, H. Q. Liu, D. P. Zhao, X. F. Zhu, A. Umar, H. Algarni and X. Wu, *ACS Appl. Nano Mater.*, 2021, **4**, 5461–5468.
23 W. H. Shi, G. Y. Han, Y. Z. Chang, H. Song, W. J. Hou and Q. Chen, *ACS Appl. Mater. Interfaces*, 2020, **12**, 45373–45382.
24 Y. Y. Zheng, J. Xu, X. S. Yang, Y. J. Zhang, Y. Y. Shang and X. Y. Hu, *Chem. Eng. J.*, 2018, **333**, 111–121.
25 J. H. Zhu, Y. Wang, X. B. Zhang and W. F. Cai, *Nanotechnology*, 2021, **32**, 145404.
26 T. F. Yi, S. Y. Qi, Y. Li, L. Y. Qiu, Y. G. Liu, Y. R. Zhu, J. H. Zhang and Y. M. Li, *Energy Technol.*, 2020, **8**, 2000096.
27 C. Liu, X. Wu and H. Xia, *CrystEngComm*, 2018, **20**, 4735–4744.
28 F. F. Zhu, W. J. Liu, Y. Liu and W. D. Shi, *Chem. Eng. J.*, 2020, **383**, 123150.
29 T. Liu, J. H. Liu, L. Y. Zhang, B. Cheng and J. G. Yu, *J. Mater. Sci. Technol.*, 2020, **47**, 113–121.
30 Z. Yuan, A. T. Zhang, D. G. Jiang, N. Mao, J. M. Tian, W. G. Huang, R. Liu and J. Q. Liu, *Chem.–Eur. J.*, 2020, **26**, 4790–4797.
31 K. H. Han, Y. Liu, H. Huang, Q. H. Gong, Z. L. Zhang and G. W. Zhou, *RSC Adv.*, 2019, **9**, 21608–21615.
32 J. Wu, S. Y. Li, P. Yang, H. P. Zhang, C. Du, J. M. Xu and K. X. Song, *J. Alloys Compd.*, 2019, **783**, 279.
33 M. M. Zhang, A. Nautiyal, H. S. Du, J. H. Li, Z. Q. Liu, X. Y. Zhang and R. G. Wang, *Electrochim. Acta*, 2020, **357**, 136877.
34 J. Li, L. Cui and X. G. Zhang, *Appl. Surf. Sci.*, 2010, **256**, 4339–4343.
35 X. X. Zhang, M. Y. Gao, L. Tong and K. F. Cai, *J. Materiomics*, 2020, **6**, 339–347.
36 X. Y. Hong, J. H. Li, G. S. Zhu, H. R. Xu, X. Y. Zhang, Y. Y. Zhao, J. Zhang, D. L. Yan and A. B. Yu, *Electrochim. Acta*, 2020, **362**, 137156.
37 Y. H. Zhao, H. X. Dong, X. Y. He, J. Yu, R. R. Chen, Q. Liu, J. Y. Liu, H. S. Zhang, R. M. Li and J. Wang, *J. Power Sources*, 2019, **438**, 227057.
38 B. Yu, G. H. Jiang, W. C. Xu, C. Cao, Y. K. Liu, N. Lei, U. Evariste and P. P Ma, *J. Alloys Compd.*, 2019, **799**, 415–424.
39 J. X. Dong, S. J. Li and Y. Ding, *J. Alloys Compd.*, 2020, **845**, 155701.
40 T. T. Bi, J. L. Jiang, Y. Lei, X. Zheng, Z. F. Jia, Z. Q. Wei and H. Yang, *Appl. Surf. Sci.*, 2020, **530**, 147317.
41 F. L. Zhao, D. Xie, W. X. Huang, X. R. Song, M. A. Z. G. Sial, H. L. Wu, F. Deng, Q. Zhang, J. Z. Zou and X. R. Zeng, *J. Colloid Interface Sci.*, 2020, **580**, 160–170.
42 X. Y. Yang, C. L. Xiang, Y. J. Zou, F. Xu, X. Q. Mao, X. B. Hu, J. Zhang and L. X. Sun, *J. Mater. Res. Technol.*, 2020, **9**, 13718–13728.
43 J. Z. Zou, D. Xie, F. L. Zhao, H. L. Wu, Y. Niu, Z. J. Li, Q. M. Zou, F. Deng, Q. Zhang and X. R. Zeng, *J. Mater. Sci.*, 2020, **56**, 1561–1576.